RESEARCH ARTICLE | JUNE 23 2025

Electrospray propulsion time-of-flight secondary ion mass spectrometry diagnostic

Giuliana C. Hofheins ; Zach Ulibarri ; Elaine M. Petro

Rev. Sci. Instrum. 96, 063306 (2025)
https://doi.org/10.1063/5.0248558

Review of Scientific Instruments ARTICLE pubs.aip.org/aip/rsi

Electrospray propulsion time-of-flight secondary ion mass spectrometry diagnostic

Cite as: Rev. Sci. Instrum. 96, 063306 (2025); doi: 10.1063/5.0248558
Submitted: 12 November 2024 • Accepted: 31 May 2025 •
Published Online: 23 June 2025

Giuliana C. Hofheins,[a] Zach Ulibarri, and Elaine M. Petro

AFFILIATIONS

Cornell University, Ithaca, New York 14850, USA

[a]Author to whom correspondence should be addressed: gch72@cornell.edu. URL: https://www.astralab.mae.cornell.edu

ABSTRACT

The design and capability of a novel electrospray propulsion time-of-flight secondary ion mass spectrometry (TOF-SIMS) diagnostic are presented to investigate secondary species emission from surface impingement of energetic molecular ion plumes. Designed on the basis of traditional SIMS principles, this diagnostic provides information on the relative intensity and chemical composition of charged secondary species given electrospray operational parameters like incident angle, primary ion energy, and target surface composition. The system consists of an externally wetted tungsten ion source operating with room temperature ionic liquid propellant, a target with a secondary species acceleration mesh, and a time-of-flight mass spectrometer with an electrostatic gate and microchannel plate detector. The results show that energetic primary plume impacts with a silver metallic surface induce both sputtering of the target (Ag^+, Ag_2^+, and Ag_3^+) and molecular secondary ion emission in both polarities. Within these secondary species, peaks related to the ionic liquid primary ions (B^+ and F^-) were definitively detected. The remaining secondary ions include fragmentation products of the EMI^+ cation, common salt contaminants (Na^+, K^+, and Cl^-), and hydrocarbon species from ambient vacuum facility conditions. The fragment pattern observed is consistent with both the ionic liquid components and typical contaminants encountered in high-vacuum TOF-SIMS analyses. For electrospray propulsion, these secondary species contribute to lifetime-limiting processes intrinsic to thruster operation, like impingement and degradation of electrodes and emitters, while also contributing to facility effects that can corrupt ground-based testing and thruster qualification.

I. INTRODUCTION

Electric space propulsion systems produce thrust via accelerating propellant through a combination of electric and magnetic fields. The fundamental advantage of electric propulsion (EP) is that the propellant exhaust velocity is determined by the applied input power rather than constrained by intrinsic chemical bond energy, thus enabling highly fuel-efficient systems for lower spacecraft propellant mass fractions.[1] Electrospray micropropulsion thrusters are a subset of electric propulsion systems that utilize electrostatic fields to extract and accelerate charged particles from a liquid propellant on either a sharp emitter tip or capillary meniscus.[2] When a potential difference on the order of a few kilovolts is applied between the emitter and a downstream extractor electrode, a Taylor cone is formed from a combination of surface tension, electric, and hydrodynamic stresses.[3,4] Therefore, ion emission is induced through field emission evaporation, where ions are subsequently accelerated to velocities exceeding 10 000 m/s.[3] This process forms polydisperse plumes ($\sum_{i=1} q_i/m_i$) that generate thrust on the order of magnitude of nanonewtons to micronewtons per emitter.[5] The composition of the plume ranges from pure ion emission[6] to larger multiply charged droplets,[7] depending on the type of emitter and operating modes.

A subset of electrospray devices utilize chemically complex molten salt propellants known as room temperature ionic liquids (RTILs), comprised of organic cations and anions. Common propellants include 1-ethyl-3-methylimidazolium tetrafluoroborate (EMI-BF_4), and 1-ethyl-3-methylimidazolium bis(trifluoromethylsulfonyl)imide (EMI-Im) as shown in Fig. 1, where the EMI^+ cation is composed of an imidazolium ring with alkyl functional groups. These propellants are attractive for electrospray propulsion devices, as they are nonvolatile and can be operated in either polarity, eliminating the need for an external neutralizer.[8] The combination of these properties makes RTIL electrospray thrusters attractive for missions requiring efficient, compact, low-mass, and low-power propulsion systems. Such examples include small satellite propulsion[9] as well as precise

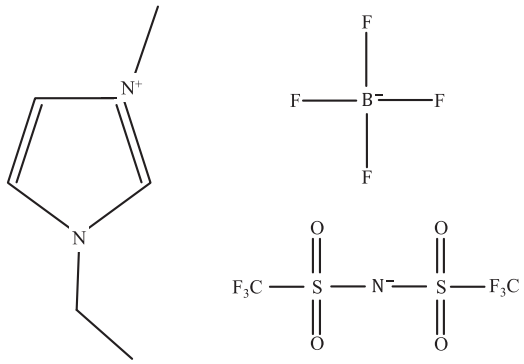

FIG. 1. Structural formulas for common ionic liquid propellants, the cation 1-ethyl-3-methylimidazolium (EMI^+), and anions tetrafluoroborate (BF_4^-) and bis(trifluoromethylsulfonyl)imide (Im−).

spacecraft control, like the LISA Pathfinder technology demonstration mission, which tested EMI-Im colloid thrusters.[10]

However, complex organic RTILs have vastly different chemical properties compared to inert noble gas electric propulsion propellants like xenon and krypton employed in ion and Hall thrusters.[1] While noble gas ion-surface interactions have decades of research due to their nearly ubiquitous use among EP systems, the surface interactions of complex ions are hypothesized to be much different.[11] For example, they may deposit at low energies or form new fragment product ions at high energies.[12] Both experiments[13] and simulations[5] indicate that particles from the plume impact thruster and spacecraft surfaces like the extractor electrode, resulting in propellant accumulation and eventual device failure.[14] However, there is a wide gap in the knowledge of the fundamental physics of these molecular ion-surface collisions at the nanoscale and how they ultimately impact thruster lifetime and performance. Moreover, these systems are tested and validated in ground-based vacuum testing environments where secondary species from plume-surface impacts are known to affect diagnostics.[15,16] Therefore, it is important to understand the chemical composition of secondary species not only for system modeling and lifetime considerations but also for facility effects on electrospray testing. The uncertainty of collision products makes it difficult to predict, correct for, and model these discrepancies.

Both numerical simulations and experimental investigations have been conducted to characterize electrospray plume-surface interactions. Molecular dynamics (MD) studies have been performed with both non-reactive[17,18] and reactive force fields[12] with EMI-BF_4 impacting various target surfaces. Bendimerad and Petro[12] produced pseudo-mass spectra of EMI-BF_4 impacting a potential wall with a reactive force field, showing the relation between the relative intensity of fragmentation products and impact energy. Experimental efforts from Uchizono *et al.*[19,20] and Klosterman *et al.*[21] have quantified secondary species yields, and Uchizono *et al.*[16] have examined the role of secondary species in experimental testing. Shaik *et al.*[22] employed a residual gas analyzer to identify secondary species from an electrospray thruster plume impinging on stainless steel. However, both MD and experimental efforts have yet to characterize the chemical composition of charged secondary species that arise from plume-surface interactions across the permutation of thruster operation variables (target surface composition, primary beam energy and current, and background pressure).

Time-of-flight secondary ion mass spectrometry (TOF-SIMS) is a standard surface composition characterization technique, commonly used in either static mode to non-destructively characterize the outermost monolayer of a sample or in dynamic mode to probe depth-based composition.[23] The general premise is to fire a high-energy ion beam (1–100 keV) at an incidence angle upon the surface of interest. This collision induces sputtering, where a fraction of the sputtered species exists as low-energy ions.[23] To form the secondary ion beam, these sputtered secondary ions are extracted and accelerated down a time-of-flight tube to a detector, where a mass spectrum of secondary ions is derived based on energy conservation.[6] The resulting spectrum gives insight into the atomic and molecular features of the sample of interest. Canonically, SIMS is employed with high-energy, large atomic number primary ion beams (Cs+, Ga+, etc.), and sputtering is most generally modeled via purely kinetic momentum transfer from isotropic collision cascades.[23] The energy of the sputtered population is generally modeled as Maxwell–Boltzmann distributions with peak energies below 10 eV and higher energy tails potentially extending to a few hundred eV from atomic secondary ion emission.[23] Alternatively, current research shows that small molecular primary ion beams (Bi_n^+, SF_5^+, In_n^+, etc.) induce kinetically assisted sputtering, as shown in Fig. 2.[24–26] This type of sputtering removes surface atoms, molecules, or ions from overlapping collisions from a singular initial collision event that induces thermal evaporation of substrate atoms and ions.[23] This method has proven not only to increase sputter yields but also the ability to detect large intact organic molecules from the target surface.[27]

The difference between a traditional TOF-SIMS and an electrospray propulsion testing lies in both the complex organic molecular composition of RTIL electrospray plumes and the typical experimental vacuum environments. These complex plumes give rise to multiple processes like deposition and fragmentation, both in the plume and upon impact.[5,12] However, work by Fujiwara and Saito[28] has proven that ionic liquids (EMI-Im) can be effective as TOF-SIMS primary ion beams. In addition, commercial TOF-SIMS are ultra-high vacuum systems ($<10^{-9}$ Torr) to mitigate background gas adsorption onto the target surface and interference with the signal.[23] Electrospray propulsion systems are tested in a range of

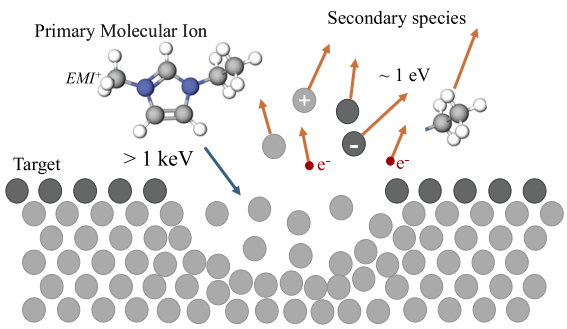

FIG. 2. Simplified kinetically assisted potential sputtering of a metallic target with a representative adsorbed monolayer (oxides, hydrocarbons, etc.).

vacuum environments, with some facility pressures orders of magnitude higher than those of commercial TOF-SIMS. This implies that in nominal test environments, an electrospray plume impacts not only bare surfaces but also those coated with adsorbed contaminants, including hydrocarbons (from pump oils and handling), as well as other common improper handling contaminants like salt ions (sodium, potassium, and chlorine) and silicones,[21,29] thereby further convoluting device performance and diagnostic evaluation.

Electrospray plumes impact surfaces at high energies (>1 keV) and, therefore, induce sputtering, with a portion of the sputtered population consisting of secondary ions. These secondary ions will interact with the electrostatic fields during thruster operation and testing. Therefore, it is important to characterize their chemical composition. To accomplish this, a novel electrospray time-of-flight secondary ion mass spectrometry (ESI TOF-SIMS) diagnostic has been developed to characterize plume-surface interactions of electrospray systems. This diagnostic will inform the relevant impact of secondary ion products from given electrospray operating conditions—including impact energy, propellant, and target surface composition. The design of the experimental diagnostic is detailed in Sec. II, with secondary ion mass spectra of both polarities from an ionic liquid primary beam impacting a metallic silver target presented and discussed in Sec. III. Finally, conclusions and future work are detailed in Sec. IV.

II. ESI TOF-SIMS DESIGN

The experimental design of the electrospray TOF-SIMS diagnostic is shown in Fig. 3. The design consists of (a) a tungsten single emitter primary electrospray ion source externally wetted with EMI-BF_4 propellant, (b) a high-voltage target assembly with a secondary ion acceleration grid, (c) an electrostatic deflection gate, (d) a time-of-flight tube, and (e) a microchannel plate detector. This diagnostic was operated in a 2 ft diameter cylindrical vacuum chamber equipped with a rotary vane roughing pump and turbomolecular vacuum pump to achieve pressures between 5×10^{-5} and 1×10^{-6} Torr. The primary molecular ion plume is first produced via the tungsten electrospray ion source. This plume impacts a target surface at a given incidence angle with an impact energy dependent on the source (V_{source}) and target (V_{target}) potentials. The high-energy impacts induce the removal of secondary electrons, atoms, molecules, and ions of both polarities from the target surface.[20] In addition, processes such as collision-induced dissociation of primary ions likely contribute to the secondary population.[12,16] These low energy (<100 eV) secondary ions, electrons, and neutrals are ejected from the target surface, typically modeled as a cosine angular distribution from the surface normal.[20,23] Secondary ions of a given polarity are selectively extracted from the sputter cloud by a potential difference between the high-voltage target surface and

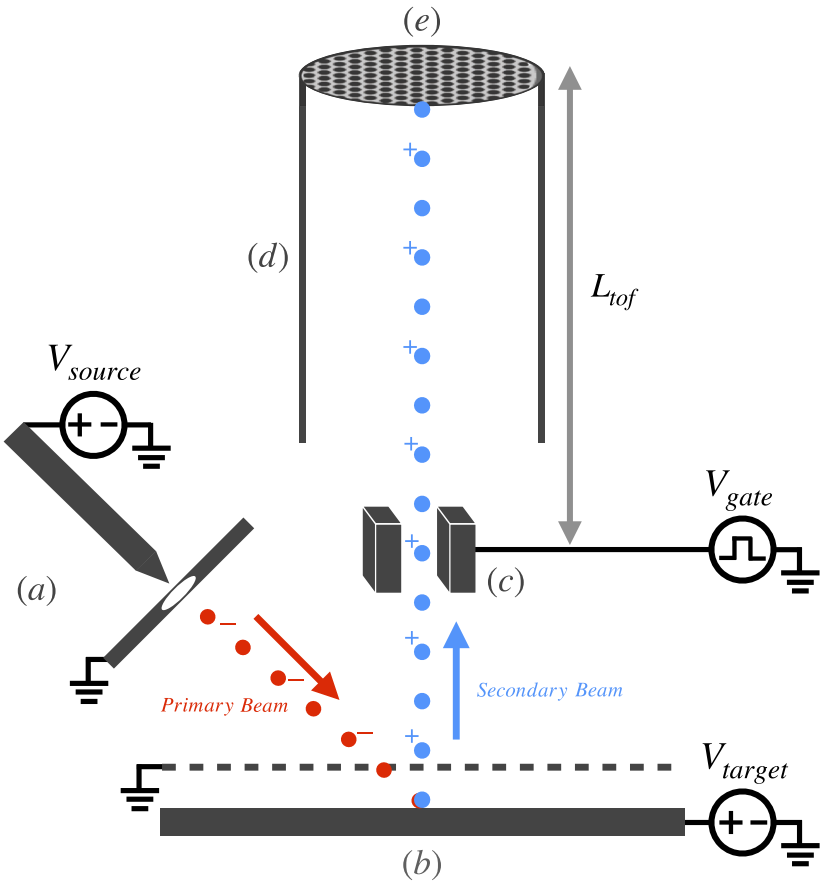

FIG. 3. The ion source (a) directs the ionic liquid primary beam at the target (b), where secondary ion emission is induced and directed toward the electrostatic gate (c) and time-of-flight system (d) with an MCP detector (e). The polarities of the two ion beams are reversed to collect negative secondary ions.

a grounded secondary ion acceleration grid. This single-polarity, approximately monoenergetic secondary ion beam passes through a pulsed high-voltage electrostatic deflection gate and down a linear time-of-flight tube. The secondary ions impact a microchannel plate detector, producing a time-of-flight curve and, therefore, a mass spectrum based on the flight time of a given species. The individual components of the electrospray TOF-SIMS system are described in further detail in Secs. II A–II C.

A. Ion source

A cross-section of the ion source employed in the diagnostic is shown in Fig. 4. The ionic liquid electrospray ion source consists of a 0.5 mm diameter tungsten rod with a tip electrochemically etched as described in Lozano and Martínez-Sánchez[6] to approximately an 8.6 μm radius of curvature as determined by approximate circular fits with a scanning electron microscope. This tungsten emitter is affixed to a dual-stage goniometer (OptoSigma GOH-40B35) via polyetheretherketone (PEEK) plates and alumina spacers (Kimball Physics) to place the needle tip at the goniometer rotation center while maintaining electrical isolation of the high-voltage electrodes from the vacuum chamber. The purpose of the goniometer is to control the pitch and yaw of the ion source while under vacuum to correct for off-axis emission, as further detailed in Ulibarri and Petro.[30] A polytetrafluoroethylene (PTFE) plate houses a stainless steel 0.125 in. outer diameter cylindrical reservoir with a porous PTFE press-fit insert for propellant retention, with propellant loading via pipette requiring ~5 μl of RTIL propellant, EMI-BF_4. A set screw from the PTFE plate's outer edge allows for electrical contact to the reservoir and, therefore, propellant. The stainless steel extractor electrode is affixed 0.15 in. from the reservoir plate, with the needle tip centered within a 0.125 in. diameter hole in the extractor.

A Taylor cone is formed on the tip of the needle by applying a high potential difference (V_{source} = ±1–3 kV) between the source and extractor under vacuum. Ion emission begins at a given startup voltage, forming a polydisperse molecular ion plume.[5] In the negative emission mode, a high negative bias is supplied to the ion source via the Keithley SourceMeter (2657A), and the extractor is grounded. This allows for the emission of negative ions, mainly in the form of BF_4^- monomers and $[BF_4^-][EMI\text{-}BF_4]$ dimers, with a fraction of the plume existing as $[BF_4^-][EMI - BF_4]_2$ trimers and higher m/z droplets. Conversely, in the positive emission mode, a high positive bias is applied to the source, with the plume consisting of EMI^+ monomers, droplets, and cationated neutrals ($[EMI^+][EMI - BF_4]_n$ with $n = 1$ dimers and $n = 2$ trimers). The masses of the plume ion species are detailed in Table I. The tungsten needle ion source employed in these experiments produces emission currents of 100–400 nA, with energy distributions of such emitters established in the literature to peak at the accelerating potential and exhibit energy distributions as detailed in Lozano,[31] with the majority of the species' energy peaking near the accelerating potential with a portion of slower fragmented species and neutrals.[31] Petro *et al.*[5] have simulated the plume divergence half angle within 7–12° from the plume centerline, with experiments showing closer to 20°.[31]

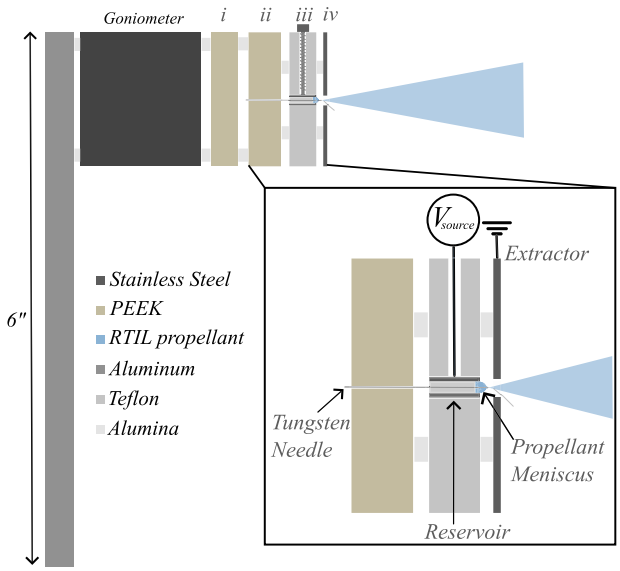

FIG. 4. Side profile cross section of the ion source, with a goniometer base, PEEK baseplates (i) and (ii), and PTFE reservoir plate (iii) with stainless steel reservoir, stainless extractor (iv), and externally wetted tungsten needle emitter.

TABLE I. Primary EMI-BF_4 ionic liquid ion plume species dependent on firing polarity, including primary monomers (n = 0) and cationated and anionated neutrals (n > 0).

Polarity	Plume species	Order	Molecular mass (amu)
+	$EMI^+(EMI\text{-}BF_4)_n$	n = 0	111
		n = 1	309
		n = 2	507
–	$BF_4^-(EMI\text{-}BF_4)_n$	n = 0	87
		n = 1	285
		n = 2	483

This ion source design allows for the adjustment of the firing angle of the tungsten source while under vacuum, thereby enabling control of off-axis emission through the use of a goniometer controlled by flexible shafts. An additional benefit of this design is a semi-consistent needle-to-extractor distance from test to test and the mitigation of propellant bubbling during vacuum pump-down. Compared to a thruster array, a single emitter allows for a more precise correlation of primary ion beam properties (current, energy spectra, and mass spectra) with secondary species.

B. Target

The electrospray plume is directed at a target biased to high voltage, V_{target}, where the impact of the primary plume and the target surface results in sputtering, or the removal of atoms, molecules, or ions from a surface.[23] The working distance measured ~2 in. from the tungsten tip to the surface. For preliminary tests, the target consisted of a 100 mm diameter silicon wafer deposited with 100 nm of silver. These wafers were created via e-beam evaporation with a CVC4500 evaporator at the Cornell NanoScale Facility. Atomically flat, uniform metallic surfaces were chosen for preliminary electrospray TOF-SIMS targets, as SIMS signals are highly sensitive to surface topology and variations in smoothness and uniformity can lead to inconsistent signals and reduce the reliability of the analysis.[23] Silver was selected as it possesses two readily identifiable

isotopes (^{107}Ag and ^{109}Ag) with nearly equal natural abundances, making it ideal for both detection and system calibration.

The secondary ion acceleration grid consists of a high-transparency (88%, TWP Inc.) stainless steel mesh grid affixed via alumina spacers 0.25 in. from the target surface. This grid is at electrical ground, creating an electric field between the target and grid that allows for (1) acceleration of the primary ions to the target and (2) simultaneous extraction of secondary ions from the sputtered cloud. Van der Heide[23] details that secondary ion energy distributions typically peak at half the surface binding energy of the target (3.1 eV for Ag), with atomic secondary ions exhibiting high-energy tails potentially extending up to 100 eV. In contrast, molecular secondary ions generally lack these high-energy emission characteristics.[23] Uchizono *et al.*[19] characterized the energy spread of secondary species from electrospray plume-surface interactions and found peaks for both polarities to peak at less than 2 eV with tails extending to 10 eV. Therefore, accelerating these secondary ions through the electric field supplied by the potential difference between the high-voltage sample and the grounded acceleration grid creates an approximately monoenergetic secondary ion beam.

An important note about this experimental setup is the polarity of the voltages on the source and target. The target is maintained at a high potential, V_{target}, with polarity opposite to the source voltage, V_{source}, resulting in a total impact energy equal to the sum of these two voltages,

$$E_{impact} = |\pm V_{source}| + |\mp V_{target}|. \tag{1}$$

It is important to note that the target bias is modular, allowing V_{target} to be adjusted according to the specific analysis. When $|\pm V_{target}| < |\pm V_{source}|$, like-polarity measurements (positive primary, positive secondary, and vice versa) are theoretically enabled. However, this configuration reduces impact energies and, therefore, secondary ion yields, lowering the intensity and signal-to-noise ratio of TOF measurements.

C. Time-of-flight mass spectrometer

The time-of-flight mass spectrometer (TOF-MS) system allows for the identification of secondary ions' mass-to-charge ratio. Time-of-flight is a standard electrospray propulsion diagnostic to determine the composition of the ion plume for indirect thrust and specific impulse measurements.[6,32] The system used for this ESI TOF-SIMS diagnostic replicates a typical in-house system used for electrospray TOF-MS, with the specific system employed in this diagnostic detailed in Cogan *et al.*[33] For electrospray TOF-SIMS, secondary ions are accelerated from the target surface to form an approximately monoenergetic secondary ion beam with an energy essentially equivalent to V_{target}, given their low ejection energies from the sample. This beam is passed through an electrostatic gate consisting of two parallel electrodes pulsed to ±950 V with a Berkeley Nucleonics PVM-4210 at a frequency of 1 kHz via a Keysight EDU33212A waveform generator. The gate alternately deflects and allows the beam to pass through at this frequency. The secondary plume travels down the TOF tube, separating the species according to the mass-to-charge (m/z) ratio. Detection occurs at the microchannel plate (Hamamatsu F12107, gain ~10^4) coupled with a transimpedance amplifier (Advanced Research Instruments Corporation TDC-30, 0.5 V/1 μA), with the signal recorded by an oscilloscope. The flight time, t_{TOF}, is the time it takes for a particle to travel from the center of the gate to the microchannel plate detector. This flight time is related to the mass of the particle, m, by conservation of energy,

$$t_{TOF} = \frac{L_{TOF}}{\sqrt{2\left(\frac{z}{m}\right)V_{target}}} + t_{delay}, \tag{2}$$

where L_{TOF} is the length of the flight tube, z is the charge state of the particle, and t_{delay} is the time delay between the oscilloscope trigger and the actual time the electrostatic gates come to high potential (typically tens to hundreds of nanoseconds). For ~1 amu mass resolution, L_{TOF} is ~1 m, but the actual flight length can vary slightly between experiments. The TOF raw signal records the current as a function of time, with each step of current indicating a species arriving at the detector.[34,35] These raw signals are averaged more than 32, 000 times during steady-state operation by the oscilloscope. The summed spectra are then data processed by a mild Gaussian blur of width 2 to make the derivative of this current trace data much more steady and consistent, as further detailed in Sec. II C 1. The derivative of the smoothed data is then used to obtain a spectral representation of the plume composition.

1. X-axis determination and peak fits

Due to the nature of the TOF-SIMS target in the vacuum chamber, accurately measuring the precise flight distance is challenging and changes slightly from experiment to experiment. The flight distance is a critical parameter in Eq. (2), which complicates the precise determination of the x-axis of the TOF mass spectra. In addition, the electrostatic gate is pulsed to a high potential by a square wave from a function generator, which also triggers the data capture via an oscilloscope. There is a time delay, t_{delay}, in Eq. (2), of hundreds of nanoseconds between the triggering square wave and the actual time when the gate comes to full potential and the gate opens or closes. This further complicates the x-axis determination.

To enable more precise x-axis determination, Exponentially modified Gaussians (EMGs) were fitted to the smoothed derivative mass lines in each spectrum, similar to the approach detailed further in Ulibarri *et al.*[36] These EMGs have the form

$$a_0 \frac{\lambda}{2} e^{\frac{\lambda}{2}(2\mu+\lambda\sigma^2-2t)} \cdot erfc\left(\frac{\mu+\lambda\sigma^2-t}{\sqrt{2}\sigma}\right), \tag{3}$$

where a_0 is the amplitude, λ is an exponential decay term, σ^2 is the variance, μ is the mean, and *erfc* is the complementary error function. Initial guess EMGs of arbitrary small amplitude and variance were visually placed at the time indices of the observed mass lines, and the SciPy curve fitting routine was then used to determine the fitted parameters for each mass line. The index of the local maximum of each resultant EMG was taken as the EMG's location, and two known or suspected mass lines were then assigned mass numbers. A simple minimization was then performed to determine which flight distance and time delay resulted in the smallest mass error for these identified lines, and the calibration can then be validated against other known mass lines to ensure proper constraints were selected. The specific mass lines chosen to constrain the x-axis are discussed in detail in Sec. III B.

III. RESULTS

A. Ion source plume composition

Direct TOF-MS analysis of the primary electrospray plume was performed to evaluate the plume composition of the single emitter ion source, as shown in Fig. 5. The raw TOF curves were smoothed with a quadratic Savitzky–Golay filter smoothed over successive five data point bins.[37] Firing in the source positive mode with V_{source} at +2 kV and L_{TOF} = 0.97 m resulted in a plume of balanced monomer/dimer composition in roughly equal proportions, with the remaining fraction consisting of trimers and higher m/z droplets. The mass-to-charge ratio of the droplet population extends to at least ~ $m/z = 10^5$, as shown by the tail of the plot in Fig. 5. This result was paralleled in the negative firing mode with V_{source} at −2 kV and L_{TOF} = 0.97 m, as shown in Fig. 5. However, the negative mode plume is composed of ~15% droplets compared to ~7% in the positive mode. Both of these confirm that the ion source operates primarily in the pure ion regime, with a population of higher mass-to-charge ratio droplets that mirrors typical compositions of ion-mode ionic liquid electrospray plumes.[6,13,34]

B. Secondary ion spectra

To demonstrate diagnostic capability, electrospray TOF-SIMS analysis was performed in both secondary ion polarities with a primary plume impact energy at 4 keV in a 5×10^{-5} Torr vacuum environment. For the positive secondary ion analysis, the source voltage, V_{source}, was held at −2 kV while the sample voltage, V_{sample}, was held at +2 kV. Similarly, V_{source} was held at +2 kV while the sample voltage, V_{sample}, was held at −2 kV for the negative secondary ion analysis. Emission currents averaged −75 ± 5 nA in the negative emission mode and 250 ± 40 nA in the positive mode .

1. Positive secondary ion spectrum

The raw time-of-flight curve for the positive secondary ions formed from a negative 4 keV EMI-BF_4 plume impacting a silver target is shown in Fig. 6. While the figure reports the normalized signal,

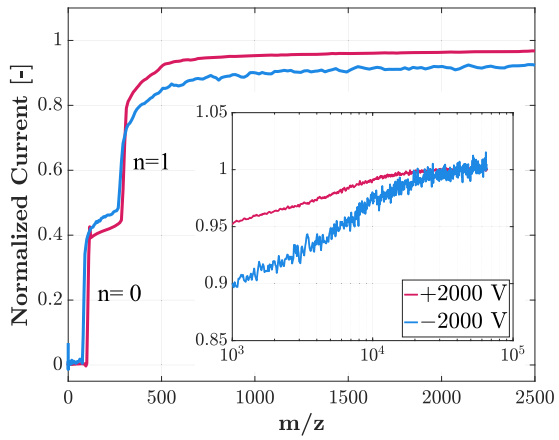

FIG. 5. Primary time-of-flight of both firing modes of the single externally wetted tungsten ion source with ±2 kV accelerating potentials, where *n* indicates the solvation order of the ions as detailed in Table I.

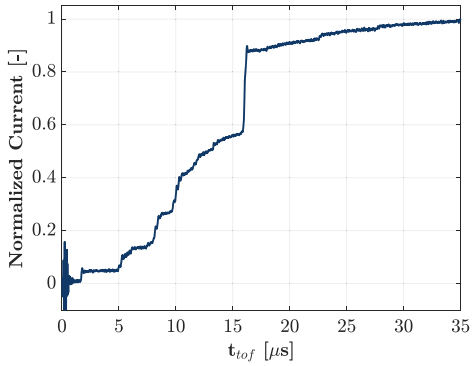

FIG. 6. Raw time-of-flight curve of positive secondary ions produced by a negative 4 keV EMI-BF_4 plume impact with an Ag target.

the maximum voltage reading on the oscilloscope read tens of millivolts, approximately one to two orders of magnitude less than typical single-volt readings for primary TOF measurements on this system. Given that this voltage corresponds to a current signal amplified by ~5 × 10^9, these voltage readings correspond to nano-to-picoamp levels of current for secondary ions reaching the MCP detector. The curve exhibits ringing and overshoot, presumably attributed to either impedance mismatching within the high-voltage circuitry or an unstable high voltage connection to the pulsed electrostatic gate.

The time-of-flight curve in Fig. 6 shows distinct arrival times of species before 30 μs, with a relatively small droplet tail extending to ~35 μs before the curve gradient converges to zero. There are six groupings of ion flight arrival times before the most intense peak at 17 μs, followed by three small yet distinct steps at 18, 23, and 28 μs. The continuous higher-mass population following these discrete features can be attributed to droplet components in the primary beam, where progeny droplets that likely result from processes like shock-induced desorption and splashing of deposited propellant upon impact are among the secondary charged species.[16]

Figure 7 shows the positive secondary ion raw time-of-flight curve as well as the smoothed derivative in the mass domain. X-axis error minimization, as detailed in Sec. II C 1, was performed for the smoothed positive ion data using an easily identifiable hydrogen line and the dominant silver isotope ion of 106.9 amu. This minimization resulted in a calculated flight distance of 0.953 m and a t_{delay} of 150 ns, which is largely consistent with other work performed with this setup.[33] Using this constrained x-axis, the second silver isotope at 109 amu is correctly identified. Importantly, silver clusters are also identified at the appropriate masses of 215 and 323 amu, indicating a good lock on the correct X-axis.

Chemical identification of the detected peaks is found in Table II, with reference detections that refer to works that have also detected the given peak in a related study. All potential peaks reported have been additionally validated as chemically viable in the NIST Chemical WebBook.[38]

The most intense peaks at m/z = 107 and 109 amu correspond to the silver isotope monomer ions ($^{107}Ag^+$ and $^{109}Ag^+$), indicating clear sputtering of the target by the primary ion beam. Further evidence of sputtered target material are the detections of silver dimers Ag_2^+ (m/z = 215 amu) and trimers Ag_3^+ (m/z = 323 amu), as shown

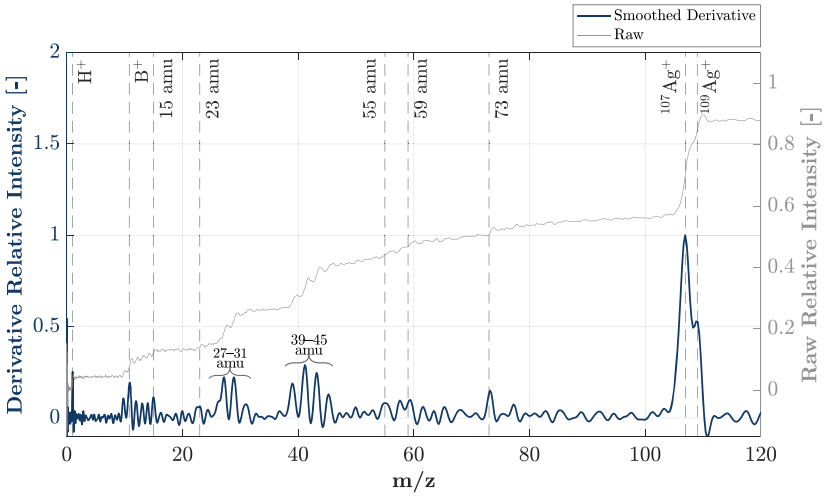

FIG. 7. Positive secondary ion mass spectrum from a 4 keV negative EMI-BF_4 plume impact with an Ag target, out to 120 amu.

in the time domain in Fig. 6 at 23 and 28 μs and in the mass domain in Fig. 8. In addition, a small peak at approximately 18 μs and t_{tof} = 18 m/z = 135 amu points to possible detection of $AgCO^+$, as detected in a TOF-SIMS study by Slusser and Winograd.[44]

TABLE II. Positive secondary ion collection mode species detection, with mass resolution +/− 1 amu.

Mass (amu)[a]	Potential species	Reference detection
1	H^+	22, 39, and 40
10	$^{10}B^+$	
11	$^{11}B^+$	
12	C^+	22 and 39
13	CH^+	22 and 39
14	CH_2^+	22 and 39
15	CH_3^+	22 and 39–41
23	Na^+	29
27	$C_2H_3^+$	39–41
29	$C_2H_5^+$, CH_3N^+, CHO^+	39–42
31	CF^+, CH_3O^+	40
39	$C_3H_3^+$, K^+	29
41	$C_3H_5^+$, $C_2H_3N^+$	39, 41, and 42
43	$C_3H_7^+$, $C_2H_3O^+$	40–42
45	$C_2H_5O^+$, CHO_2^+, CH_3NO^+	
55	$C_4H_7^+$, $C_3H_6N^+$, CN_2O^+	41 and 42
57	$C_4H_9^+$, $C_2H_5N_2^+$	43
59	$C_4H_{11}^+$	43
73	$C_3H_5O_2^+$, $C_3H_9N_2^+$	
107	$^{107}Ag^+$	
109	$^{109}Ag^+$	
135	$AgCO^+$	44
215	Ag_2^+	
323	Ag_3^+	

[a]Assuming singly charged species.

The other notable feature of the positive secondary ion spectra is the distinct lower m/z spectral "families," characteristic of complex molecular ion fragmentation patterns. Each familial peak corresponds to a methyl group loss from the most massive group (m/z ~ 55 amu) to the least (m/z = 27 amu), with peaks within a few amu within each family. Chemically, this represents molecules with similar structural compositions.

There exist six distinct spectral positive secondary ion groupings below 100 amu, with relatively intense peaks at m/z = 1, 11, 27, 41, 58, and 73 amu. The singular peak at 1 amu corresponds to the hydrogen cation (H^+), followed by successive peaks from m/z = 10–15 amu. The detection of boron isotope ions at m/z = 10 and 11 amu is particularly significant. These peaks display a relative intensity ratio consistent with the natural isotopic abundance of boron (~1:4 for $^{10}B^+$ compared to $^{11}B^+$). Given that the primary ion beam firing polarity is negative in this ESI TOF-SIMS mode (emitting BF_4^- ions), the presence of boron in the positive secondary ions strongly suggests these ions originate from fragmentation of the

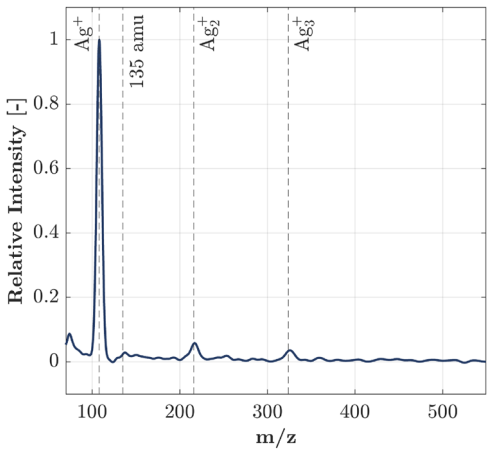

FIG. 8. Higher mass positive secondary ion mass spectrum, from 70 to 500 amu, with a Gaussian blur of width 10 to more readily see the higher mass features.

primary beam species upon impact. Methyl-related fragment ions (C^+, CH^+, CH_2^+, and CH_3^+) are detected at m/z = 12–15 amu, originating from the EMI^+ cation upon impact or from sputtered absorbed hydrocarbon gas. The peak at m/z = 23 amu suggests the presence of the sodium ion (Na^+), a common salt surface contaminant in SIMS studies that readily forms positive ions even in trace quantities.[29]

The spectral families with relatively intense peaks at m/z = 27, 41, and 58 are typically seen in many organic mass spectra,[43] including commercial TOF-SIMS of ionic liquids with imidazolium ring cations,[40,41] residual gas analyzer studies of neutral particles produced by electrospray plume impacts with stainless steel,[22] and collision-induced dissociation studies of EMI-BF_4.[42] Bundaleski *et al.*,[41] in commercial TOF-SIMS of an EMI containing ionic liquid thin film, report masses m/z = 27, 29 as the ethyl alkyl functional group fragments ($C_2H_3^+$ and $C_2H_5^+$), as well as m/z = 41, 56 as two bond scissions of the imidazolium ring ($C_2H_3N^+$ and $C_3H_6N^+$, respectively). In addition, the presence of contaminant potassium ions likely contributes to the m/z = 39 peak.

However, the m/z = 55–60 amu range notably lacks the distinct peak resolution seen in other mass regions. This spectral broadening likely results from multiple fragment species with nearly identical masses arriving simultaneously at the detector, causing signal overlap and reduced peak definition. The distinct peak at m/z = 73 amu is not observed in other RTIL related works, but potential species are listed in Table II.

These peaks also appear as secondary ions from hydrocarbon-containing materials. Surface analysis research has established that without rigorous decontamination protocols and ultra-high vacuum storage, surfaces typically acquire layers of hydrocarbons, salts, and oxides.[21,29] Multiple factors likely contribute to these contaminants in the described system: the relatively high vacuum pressure facilitating gas adsorbate formation, hydrocarbons from backstreaming vacuum pump oil, and salt ions (Na^+, K^+, and Cl^-) from improper rinsing or sample handling, all of which are recognized challenges in TOF-SIMS analysis.[29,45] Several detected peaks (m/z = 41, 43, 58) likely contain contributions from both EMI^+ fragmentation and hydrocarbon secondary ions ($C_nH_m^+$, $n \geq 2$) that cannot be derived solely from the EMI^+ cation, particularly from its ethyl functional group. The presence of common salt contaminants is further evidenced by the detection of sodium (Na^+) at m/z = 23 amu and the likely contribution of potassium (K^+) to the peak at m/z = 39 amu.

In summary, the detected positive secondary ion peaks correlate with typical fragments of the primary EMI^+ molecule, common salt contaminants (Na^+ and K^+), and characteristic fragmentation patterns of hydrocarbon species present on the target surface's outermost layer.

2. Negative secondary ion spectrum

The raw time-of-flight curve for the negative secondary ions formed from a 4 keV positive EMI-BF_4 plume impacting a silver target is shown in Fig. 9. The raw oscilloscope voltage readings corresponding to amplified current signals showed a peak of several hundred millivolts for the negative secondary ions, with an average signal strength 2.8 times higher than that of the positive secondary ions (0.15 vs 0.053 V). Compared to the positive raw spectra in Fig. 6, the negative secondary ions are lighter in mass, with the bulk

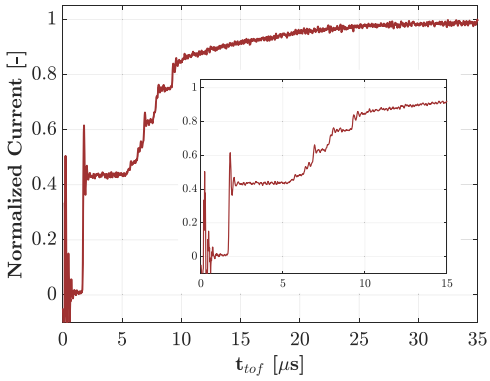

FIG. 9. Raw time-of-flight measurement of negative secondary ions produced by a 4 keV positive EMI-BF_4 plume impact with an Ag target.

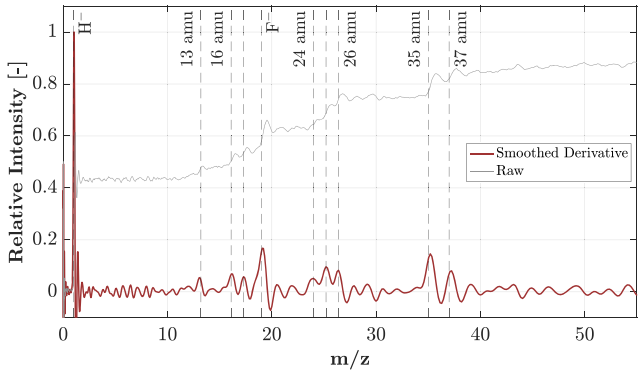

FIG. 10. Negative secondary ion mass spectra from a 4 keV positive EMI-BF_4 plume impacting an Ag target.

molecular ions having flight times of less than 10 μs. The negative droplet population also extends to a similar mass range as the positive spectra, with the population extending to ~30 μs.

The derivative of the smoothed time-of-flight curve, converted to the mass domain, of the negative secondary ions is shown in Fig. 10, with species identification detailed in Table III. The spectrum has an intense peak at m/z = 1 amu, or the hydrogen anion (H^-), as seen in other organic and RTIL-related works.[41,45] The second most intense peak at m/z = 19 amu shows the presence of the fluoride anion and is another definitive sign of the primary ionic liquid within the secondary ion species, likely originating from the BF_4 anion. The X-axis determination for negative ion data remains consistent with that of positive ions, as both datasets were collected during the same experiment. Applying the flight distance and t_{delay} parameters from the positive ion mode yields an excellent fit to the negative ion data, with dominant spectral lines observed at 1 amu for H^- and 19 amu for F^-. Importantly, attempts to minimize based on these negative ion lines do not result in significant changes to the X-axis parameters, validating the consistency of our calibration approach.

Four other spectral groupings are shown, with peaks at m/z = 13 (CH^-) and 24, 25, 26 (C^-, CH^-, and CH_2^-) related

TABLE III. Negative secondary ion collection mode species detection, with mass resolution +/− 1 amu.

Mass (amu)[a]	Potential species	Reference detection
1	H^-	41 and 45
12	C^-	39 and 45
13	CH^-	39 and 45
16	O^-	41 and 45
17	OH^-	41 and 45
19	F^-	40 and 41
24	C_2^-	39, 41, and 45
25	C_2H^-	39, 41, and 45
26	$C_2H_2^-$	40, 41, and 45
35	$^{35}Cl^-$	29
37	$^{37}Cl^-$	29

[a]Assuming singly charged species.

to hydrocarbon secondary ions from fragmented EMI^+[39,41] and/or adsorbed hydrocarbon contamination.[45] Peaks likely related to water and oxide layers are found at m/z = 16, 17 amu (O^- and OH^-), as seen in Van Stipdonk *et al.*[45] The peak at 26 amu may also reflect CN^- secondary ions, as seen in Bundaleski *et al.*[41] The peaks observed at m/z = 35, 37 amu are likely the chlorine isotopes ($^{35}Cl^-$ and $^{37}Cl^-$) that are common contaminants found in SIMS studies.[29] These peaks display a relative intensity ratio roughly consistent with the natural isotopic abundance of chlorine (~3:1 for $^{35}Cl^-$ compared to $^{37}Cl^-$), further confirming this assignment.

IV. CONCLUSION

A novel electrospray time-of-flight secondary ion mass spectrometry diagnostic was experimentally validated to probe the chemical composition of secondary ion mass-to-charge ratios from plume-surface impacts. This was achieved via a single externally wetted tungsten electrospray ion source operating with room temperature ionic liquid propellant, EMI-BF_4, in a ~10^{-5} Torr vacuum testing facility. Impacts of the primary plume with a silver target induced secondary ion emission characterized by time-of-flight mass spectrometry. Positive secondary ion mass spectra showed clear evidence of target sputtering through detection of silver isotopes ($^{107}Ag^+$ and $^{109}Ag^+$) and silver clusters (Ag_2^+ and Ag_3^+), along with definitive signs of propellant fragmentation through boron isotopes ($^{10}B^+$ and $^{11}B^+$). The spectra also revealed typical SIMS contaminants (Na^+ and K^+) and fragment patterns consistent with both EMI^+ fragmentation and hydrocarbon contaminants.

In the negative secondary ion spectrum, the signal was dominated by H^- ions but displayed strong F^- signals and chloride isotopes in the correct relative abundances ($^{35}C^-$ and $^{37}C^-$), demonstrating the presence of both propellant fragments and surface contaminants. Additional ion species with m/z values below 40 amu were detected in both polarities, most likely related to hydrocarbon and primary ion impact fragmentation products. For both spectra, the detected species are of significant interest as they result from opposite polarity primary plume impacts and are the most likely to backstream and contribute to lifetime-limiting processes.

It is important to note that this diagnostic can be replicated using standard instruments commonly found in electric propulsion laboratories, enabling the study of a wide range of plume-surface interactions. While the described diagnostic utilizes a microchannel plate detector—a current-collecting electrode paired with a transimpedance amplifier that offers sufficient gain and a strong signal-to-noise ratio could also be effective, as demonstrated in systems like Lyne *et al.*[32] In addition, this diagnostic is source-agnostic, meaning the single emitter in this study can be replaced with emitter arrays and thrusters or different types of emitters across the spectrum of electrospray variants (such as capillary and porous emitters). Given that surface processes vary based on the primary plume composition,[16] the resulting secondary species composition is likely to differ depending on the source and target composition. This diagnostic flexibility is particularly crucial for facility calibrations, as it enhances the understanding of the secondary species populations generated from plume interactions with vacuum chamber surfaces and how those secondary ions influence electrospray operation as well as other diagnostics.

Future work will focus on determining the source of secondary ions—whether from target-based contamination or primary plume fragmentation. This information will be critical in determining relevant secondary ion species in terms of intrinsic thruster operation or facility effects. In addition, it will be important to also characterize like-polarity secondary ions as the primary plume to understand secondary ion generation. While Ref. 46 has shown that there is ESI TOF-SIMS signal degradation below impact energies of 2 keV that prevents clear time-of-flight signals in the presented diagnostic configuration, like-polarity spectra could likely be achieved with this same diagnostic framework but with the addition of an accelerating stage to the ion source and biasing the target in the same polarity as the firing polarity. This method is reserved for future work. With this approach, the diagnostic can then be applied to test the permutation of thruster operating conditions, propellants, and surfaces of interest for a comprehensive electrospray TOF-SIMS analysis of electrospray thruster plume-surface interactions.

Electrospray propulsion devices show promise to be mission-enabling technologies. Characterizing secondary ions that form via plume-surface interactions will enable both high-fidelity flight qualification tests and thruster operations, as well as inform secondary species mitigation techniques.

ACKNOWLEDGMENTS

This work was supported by a NASA Space Technology Graduate Research Opportunity fellowship (80NSSC23K1212). This work was supported in part by the Heising Simons Foundation 51 Pegasi B Fellowship Grant No. 2024-5175. A portion of this work was supported by a grant from the Jet Propulsion Laboratory, California Institute of Technology, under contract with the National Aeronautics and Space Administration (Grant No. 80NM0018D0004). This work was performed in part at the Cornell NanoScale Facility, an NNCI member supported by NSF Grant NNCI-2025233.

AUTHOR DECLARATIONS

Conflict of Interest

The authors have no conflicts to disclose.

Author Contributions

Giuliana C. Hofheins: Conceptualization (lead); Data curation (lead); Formal analysis (lead); Funding acquisition (lead); Investigation (lead); Methodology (lead); Validation (lead); Visualization (lead); Writing – original draft (lead); Writing – review & editing (lead). **Zach Ulibarri**: Conceptualization (supporting); Formal analysis (supporting); Investigation (supporting); Methodology (supporting); Software (equal); Writing – review & editing (supporting). **Elaine M. Petro**: Conceptualization (equal); Funding acquisition (equal); Methodology (equal); Project administration (equal); Resources (equal); Writing – review & editing (equal).

DATA AVAILABILITY

The data that support the findings of this study are available from the corresponding author upon reasonable request.

REFERENCES

[1] D. M. Goebel, I. Katz, and I. G. Mikellides, *Fundamentals of Electric Propulsion* (John Wiley & Sons, 2023).
[2] P. C. Lozano, M. Martínez-Sánchez, and V. Hruby, "Electrospray propulsion," in *Encyclopedia of Aerospace Engineering* (John Wiley & Sons, Ltd, 2010).
[3] E. M. Petro, A. Bruno, P. Lozano, L. E. Perna, and D. Freeman, in *AIAA Propulsion and Energy 2020 Forum, AIAA Propulsion and Energy Forum* (American Institute of Aeronautics and Astronautics, 2020).
[4] X. Gallud and P. C. Lozano, J. Fluid Mech. **933**, A43 (2022).
[5] E. M. Petro, X. Gallud, S. K. Hampl, M. Schroeder, C. Geiger, and P. C. Lozano, J. Appl. Phys. **131**, 193301 (2022).
[6] P. Lozano and M. Martínez-Sánchez, J. Colloid Interface Sci. **282**, 415 (2005).
[7] V. Hruby, M. Gamero-Castano, D. Spence, C. Gasdaska, N. Demmons, R. McCormick, P. Falkos, J. Young, and W. Connolly, in *2004 IEEE Aerospace Conference Proceedings (IEEE Cat. No.04TH8720)* (IEEE, 2004), Vol. 1, p. 213.
[8] P. C. Lozano, B. L. Wardle, P. Moloney, and S. Rawal, MRS Bull. **40**, 842 (2015).
[9] F. Mier-Hicks and P. C. Lozano, J. Guid., Control, Dyn. **40**, 642 (2017).
[10] J. K. Ziemer, T. M. Randolph, G. W. Franklin, V. Hruby, D. Spence, N. Demmons, T. Roy, E. Ehrbar, J. Zwahlen, R. Martin, and W. Connolly, in *2010 IEEE Aerospace Conference* (IEEE, 2010), pp. 1–19.
[11] R. D. Kolasinski, "Fundamental ion-surface interactions in plasma thrusters," Ph.D. thesis (California Institute of Technology, 2007).
[12] R. Bendimerad and E. Petro, J. Electr. Propul. **1**, 27 (2022).
[13] D. Krejci, F. Mier-Hicks, R. Thomas, T. Haag, and P. Lozano, J. Spacecr. Rockets **54**, 447 (2017).
[14] A. Thuppul, P. L. Wright, A. L. Collins, J. K. Ziemer, and R. E. Wirz, Aerospace **7**, 108 (2020).
[15] C. Ma, V. Messina, C. N. Ryan, J. L. Rovey, Z. Putnam, M. Lembeck, and S. Berg, in *37th International Electric Propulsion Conference* (Electric Propulsion Society, 2022).
[16] N. M. Uchizono, A. L. Collins, C. Marrese-Reading, S. M. Arestie, J. K. Ziemer, and R. E. Wirz, J. Appl. Phys. **130**, 143301 (2021).
[17] N. Takahashi and P. Lozano, "Atomistic numerical approach to ion evaporation from a tungsten surface for electrospray thrusters," in 45th AIAA/ASME/SAE/ASEE Joint Propulsion Conference & Exhibit, 2009.
[18] X. G. Cidoncha, P. C. Lozano, R. Bendimerad, E. M. Petro, and S. K. Hampl, in *2022 IEEE Aerospace Conference (AERO)* (IEEE, 2022), pp. 1–11.
[19] N. M. Uchizono, C. Marrese-Reading, S. M. Arestie, A. L. Collins, J. K. Ziemer, and R. E. Wirz, Appl. Phys. Lett. **121**, 074103 (2022).
[20] N. M. Uchizono and R. E. Wirz, "Secondary species emission and behavior for electrospray thrusters," Ph.D. thesis, University of California, Los Angeles, 2022.
[21] M. R. Klosterman, J. L. Rovey, and D. A. Levin, J. Appl. Phys. **131**, 243302 (2022).
[22] S. Z. Shaik, A. R. Bendimerad, A. T. M. Tahsin, A. Smith, P. Lozano, and E. Petro, in *AIAA SCITECH 2024 Forum, AIAA SciTech Forum* (American Institute of Aeronautics and Astronautics, 2024).
[23] P. Van der Heide, *Secondary Ion Mass Spectrometry: An Introduction to Principles and Practices* (John Wiley & Sons, Inc, 2014).
[24] R. Van Ham, L. Van Vaeck, F. Adams, and A. Adriaens, J. Anal. At. Spectrom. **20**, 1088 (2005).
[25] E. R. Fuoco, G. Gillen, M. B. J. Wijesundara, W. E. Wallace, and L. Hanley, J. Phys. Chem. B **105**, 3950 (2001).
[26] J. A. Townes, A. K. White, E. N. Wiggins, K. D. Krantzman, B. J. Garrison, and N. Winograd, J. Phys. Chem. A **103**, 4587 (1999).
[27] G. Gillen and S. Roberson, Rapid Commun. Mass Spectrom. **12**, 1303 (1998).
[28] Y. Fujiwara and N. Saito, Surf. Interface Anal. **46**, 348 (2014).
[29] D. J. Graham and L. J. Gamble, Biointerphases **18**, 021201 (2023).
[30] Z. Ulibarri and E. Petro, Rev. Sci. Instrum. **96**(4), 043301 (2025).
[31] P. C. Lozano, J. Phys. D: Appl. Phys. **39**, 126 (2005).
[32] C. T. Lyne, M. F. Liu, and J. L. Rovey, J.Electr. Propul. **2**, 13 (2023).
[33] S. P. Cogan, Z. Ulibarri, E. Petro, and A. E. Hofmann, in *2023 IEEE Aerospace Conference* (IEEE, 2023), pp. 1–7.
[34] O. Jia-Richards, J. Appl. Phys. **132**, 074501 (2022).
[35] E. M. Petro, M. Cezairli, M. Schroeder, and P. Lozano, in *International Electric Propulsion Conference 2019* (Electric Propulsion Society, 2019).
[36] Z. Ulibarri, T. Munsat, M. Voss, J. Fontanese, M. Horányi, S. Kempf, and Z. Sternovsky, Icarus **391**, 115319 (2023).
[37] A. Savitzky and M. J. E. Golay, Anal. Chem. **36**, 1627 (1964).
[38] *NIST Chemistry WebBook*, edited by, P. J. Linstrom and W. G. Mallard (National Institute of Standards and Technology, Gaithersburg, MD 20899, 2019) retrieved 9 June, 2024.
[39] M. Holzweber, E. Pittenauer, and H. Hutter, J. Mass Spectrom. **45**, 1104 (2010).
[40] J. Günster, O. Höfft, S. Krischok, and R. Souda, Surf. Sci. **602**, 3403 (2008).
[41] N. Bundaleski, S. Caporali, S. P. Chenakin, A. M. C. Moutinho, O. M. N. D. Teodoro, and A. Tolstogouzov, Int. J. Mass Spectrom. **353**, 19 (2013).
[42] S. Bell, A. Taqui, M. Tahsin, and E. M. Petro, in *38th International Electric Propulsion Conference 2024* (Electric Propulsion Society, 2024) (IEPC-2024-735).
[43] P. W. F. Arisz, J. B. M. Pureveen, and R. M. A. Heeren, J. Am. Soc. Mass Spectrom. **31**, 2356 (2020).
[44] G. J. Slusser and N. Winograd, Surf. Sci. **95**, 53 (1980).
[45] M. J. Van Stipdonk, V. Santiago, and E. A. Schweikert, J. Mass Spectrom. **34**, 554 (1999).
[46] G. C. Hofheins, H. Sherman, A. Schaldenbrand, and E. M. Petro, in *AIAA SCITECH 2025 Forum* (AIAA, 2025), p. 2383.